

# Optical design and experimental characterization of a solar concentrating dish system for fuel production via thermochemical redox cycles

Fabian Dähler<sup>a</sup>, Michael Wild<sup>a</sup>, Remo Schächli<sup>a</sup>, Philipp Haueter<sup>a</sup>, Thomas Cooper<sup>a</sup>, Philipp Good<sup>a</sup>, Carlos Larrea<sup>a</sup>, Max Schmitz<sup>a</sup>, Philipp Furler<sup>a,b,\*</sup>, Aldo Steinfeld<sup>a,\*</sup>

<sup>a</sup> ETH Zurich, Dept. of Mechanical and Process Engineering, 8092 Zurich, Switzerland

<sup>b</sup> Sunredox LLC, ETH Zurich, 8092 Zurich, Switzerland

## ARTICLE INFO

### Keywords:

Solar  
Concentrator  
Optics  
Thermochemical  
Redox  
Fuel  
Reactor

## ABSTRACT

The design, fabrication, and on-sun characterization of a solar dish concentrating system for performing the two-step thermochemical redox splitting of H<sub>2</sub>O and CO<sub>2</sub> is presented. It comprises a primary sun-tracking 4.4 m-dia. solar dish concentrator coupled to a secondary planar rotating reflector. This optical arrangement enables the operation of two (or more) solar reactors side-by-side for performing both redox reactions simultaneously by alternating the solar input between them while making continuous and uninterrupted use of the incoming concentrated sunlight. On-sun characterization of the complete concentrating system revealed a peak solar concentration ratio of 5010 suns and an average of 2710 suns measured over the 30 mm-radius aperture of the solar reactor. A detailed optical analysis elucidates measures to increase the optical efficiency and concentration ratio.

## 1. Introduction

Solar splitting of H<sub>2</sub>O and CO<sub>2</sub> is performed using a thermochemical cycle based on the reduction-oxidation (redox) of metal oxides (Romero and Steinfeld, 2012), comprising two steps: (1) a high-temperature solar endothermic reduction step, and (2) a subsequent low-temperature exothermic oxidation step with CO<sub>2</sub> or H<sub>2</sub>O to generate H<sub>2</sub> and CO – syngas, the precursor of liquid hydrocarbon fuels. In the framework of the EU-project SOLARJET, we have experimentally demonstrated, at lab scale, the first ever production of solar jet fuel from H<sub>2</sub>O and CO<sub>2</sub> via such a thermochemical redox cycle (Marxer et al., 2015). In this two-step cyclic process, only the first endothermic step requires concentrated solar energy as the source of high-temperature process heat. By operating two or more solar reactors side-by-side and alternating the solar input between them, it is possible to perform both redox reactions simultaneously but separately in each reactor while making uninterrupted use of the incoming solar radiation.

Ceria (CeO<sub>2</sub>) has emerged as the benchmark redox material because of its fast reaction kinetics and crystallographic stability (Chueh et al., 2010). Its thermal reduction proceeds to a reasonable extent at a temperature of 1500 °C (Panlener et al., 1975; Scheffe and Steinfeld, 2012). This corresponds to a required solar concentration ratio<sup>1</sup> above 2000

suns for efficient operation (Romero and Steinfeld, 2012), which can be obtained by point-focus concentrating systems, either in centralized solar towers or decentralized solar dishes. In general, solar dish systems can reach higher concentrations and higher optical efficiencies compared to solar towers, but are limited to smaller unit sizes. In contrast, line-focus trough and Fresnel systems are theoretically bounded by the much lower 2D-concentration limit of 215 suns compared to the 3D-concentration limit of 46,250 suns (Winston, 1970), and are thus unsuitable for achieving the temperatures required for thermochemical redox cycles.

In this paper, we present the design, fabrication, and characterization of a high-flux solar dish system that enables the operation of two adjacent solar reactors performing both steps of the ceria-based redox cycle simultaneously while utilizing the incoming solar radiation uninterruptedly.

## 2. Optical design

Fig. 1 depicts various optical design configurations for the solar concentrating dish system for the simultaneous operation of two or more adjacent solar reactors. Table 1 summarizes the corresponding key parameters. To ensure comparability of all designs, the primary

\* Corresponding authors at: ETH Zurich, Dept. of Mechanical and Process Engineering, 8092 Zurich, Switzerland.

E-mail addresses: [furlerp@ethz.ch](mailto:furlerp@ethz.ch) (P. Furler), [aldo.steinfeld@ethz.ch](mailto:aldo.steinfeld@ethz.ch) (A. Steinfeld).

<sup>1</sup> The mean solar concentration ratio  $C_{\text{mean}}$  is defined as  $C_{\text{mean}} = \dot{Q}_{\text{reactor}} / (A_{\text{reactor}} E_{\text{bn}})$ , where  $\dot{Q}_{\text{reactor}}$  is the solar radiative power intercepted by a reactor aperture of area  $A_{\text{reactor}}$  normalized to the direct normal beam irradiance (DNI)  $E_{\text{bn}}$ .  $C_{\text{mean}}$  is often expressed in units of “suns”.

**Nomenclature***Latin characters*

$A_{\text{reactor}}$	solar reactor aperture area, m <sup>2</sup>
$A_{\text{dish}}$	dish aperture area, m <sup>2</sup>
$C_{\text{mean}}$	mean solar concentration ratio over a given area, suns
$c_p$	mass-specific heat capacity of the calorimeter cooling water, kJ/(kg K)
$C_{\text{peak}}$	peak solar concentration ratio, suns
$E_{\text{bn}}$	direct normal beam irradiance (DNI), W m <sup>-2</sup>
$f$	focal length, m
$\dot{Q}$	solar radiative power, W
$\dot{Q}_{\text{cal}}$	solar radiative power incident at calorimeter aperture, W
$\dot{Q}_{\text{dish}}$	solar radiative power incident at solar dish aperture, W
$\dot{Q}_{\text{reactor}}$	solar radiative power incident at solar reactor aperture, W
$r$	radius, m
$R_f$	radial displacement of focal point away from central axis, m
$R_i$	inner dish truncation radius, m
$R_o$	outer dish radius, m
$R_r$	outer reactor shell radius, m
$T_{\text{in}}$	calorimeter inlet temperature, °C
$T_{\text{out}}$	calorimeter outlet temperature, °C

*Greek characters*

$\alpha$	absorptance, %
$\beta$	angle between optical axis before and after reflection at secondary reflector, °
$\gamma$	intercept factor, %
$\zeta$	active area fraction, %
$\eta_{\text{opt}}$	optical efficiency, %
$\theta_{\text{off}}$	tracking offset, °
$\theta_{\text{os}}$	oversizing angle for secondary dish, °
$\theta_{\text{sun}}$	angular radius of the solar disk, 4.65 mrad
$\rho$	reflectance, %
$\sigma$	standard deviation of reflector slope error, mrad
$\phi$	rim angle, °

*Subscripts*

1	primary reflector
2	secondary reflector
f	focus

*Abbreviations*

DNI	direct normal irradiance, W/m <sup>2</sup>
SMS	simultaneous multiple surface optical design method

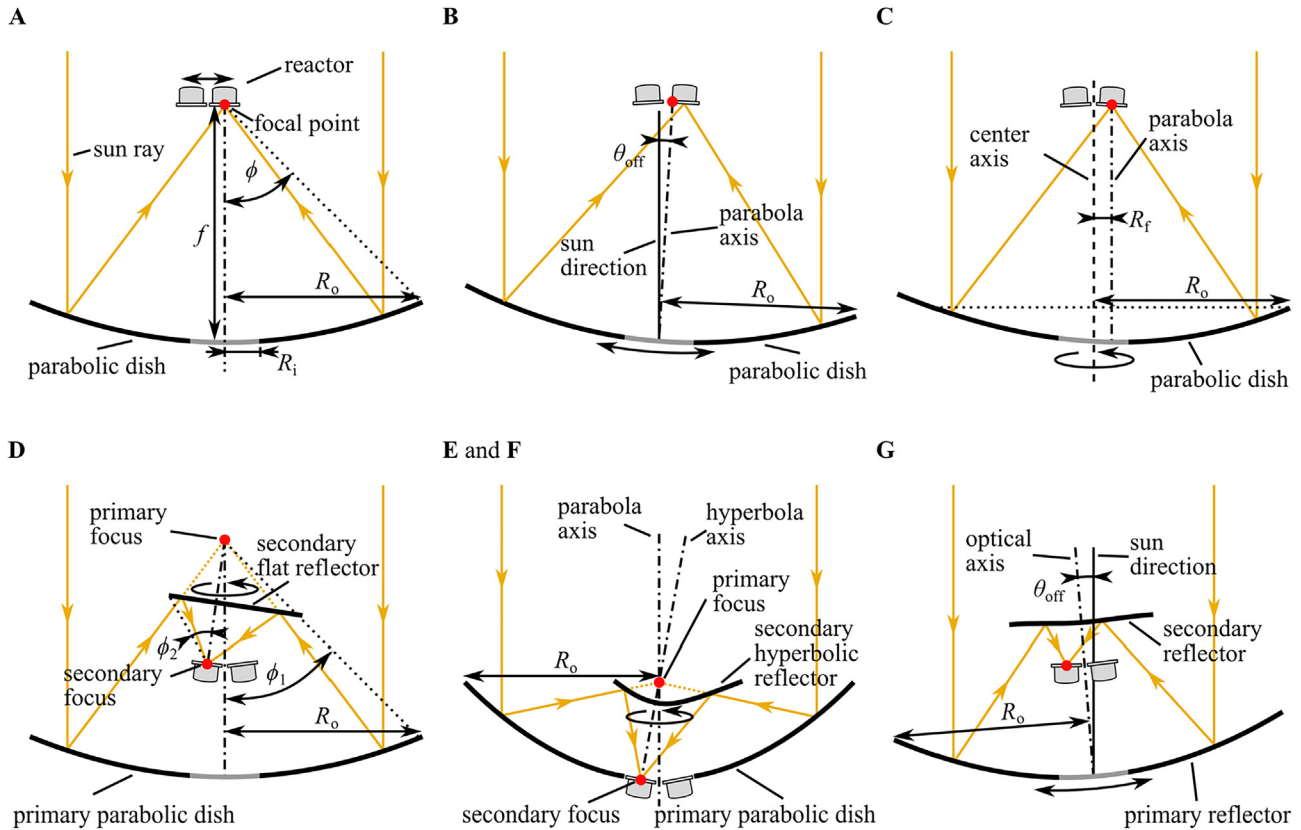


**Fig. 1.** Optical design configurations of the solar concentrating dish system for the simultaneous operation of two or more adjacent solar reactors. A–E: Primary parabolic dish with  $R_o = 2.2$  m,  $\phi = 45^\circ$  and  $f = 2.65$  m; F: primary parabolic dish with  $R_o = 2.2$  m,  $\phi = 90^\circ$ , and  $f = 1.1$  m; G: revolved free-form curve. A–C use a single primary reflector; D–G use both primary and secondary reflectors. The focal point is shifted by moving the solar reactors (A), introducing a tracking offset  $\theta_{\text{off}} = 4^\circ$  (B and G), rotating primary reflector (C), and rotating secondary reflector (D–F).

**Table 1**

Optical design configurations, the number of reflections rays undergo before hitting the solar reactor's aperture, the mechanism used to switch between the two solar reactors, the rim-angle  $\phi$ , the peak solar concentration ratio  $C_{\text{peak}}$  and the mean solar concentration ratio over a 30-mm-radius aperture  $C_{\text{mean}}$ .

Label	Design	No. of reflections	Switching mechanism	$\phi$	$C_{\text{peak}}$ [suns]	$C_{\text{mean}}$ [suns]
A	Parabolic dish	1	Move solar reactors	45°	11,100	4200
B	Parabolic dish	1	Tracking offset	45°	5100	2600
C	Asymmetric parabolic dish	1	Rotate primary	45°	11,100	4200
D	Primary parabolic dish + secondary tilted flat	2	Rotate secondary	45°/45°	8300	3300
E	Primary (low rim-angle) parabolic + secondary hyperbolic	2	Rotate secondary	45°/30°	3600	2200
F	Primary (high rim-angle) parabolic + secondary hyperbolic	2	Rotate secondary	90°/30°	3900	2400
G	Revolved free-form curve	2	Tracking offset	~50°	7200	3200

solar dish has an inner radius  $R_i = 0.4$  m and outer radius  $R_o = 2.2$  m, resulting in an inlet aperture area of  $A_{\text{dish}} = 14.7$  m<sup>2</sup>. Assuming an optical efficiency of  $\eta_{\text{opt}} = 60\%$  and incident direct normal irradiance (DNI) in the range  $600 \text{ W m}^{-2} < E_{\text{bn}} < 1000 \text{ W m}^{-2}$ , the solar radiative power expected to be delivered by the dish ranges between  $5.3 \text{ kW} < \dot{Q}_{\text{reactor}} < 8.8 \text{ kW}$ . Each solar reactor is assumed to be a cavity-receiver with a 30 mm-radius aperture and an outer shell radius  $R_r = 200$  mm. Thus, the focal point needs to be shifted by at least  $R_f = R_r = 200$  mm from the primary center axis.

Designs A to C are based on a single parabolic dish without secondary reflector while designs D to G use a primary dish and a secondary reflector. Note that the main purpose of the secondary reflector is to facilitate the moving of the focal spot between the two solar reactors. For collecting radiation spillage or increasing the solar flux concentration, a non-imaging optical stage incorporated in front of the solar reactor's aperture might be envisioned, which is however not considered here. All primary and secondary reflectors are surfaces of revolution, some of them asymmetrically truncated (primary in C, secondary in D, E, F). For A to F, the primary reflector is based on a paraboloid of revolution, while design G is based on a revolved free-form curve. All designs are benchmarked against design A: a paraboloid of revolution with a rim-angle  $\phi = 45^\circ$  which yields the theoretical maximum mean concentration ratio for a concave concentrator, 11,562 suns for full collection (peak 23,124 suns) assuming perfect geometry and reflectance (Bliss, 1957; Harper et al., 1976). For A, the solar reactors are alternately moved back and forth into the focal spot of the primary reflector. Similarly to A, B comprises a single primary parabolic reflector with rim-angle  $\phi = 45^\circ$ , but the focal point is shifted by introducing a tracking offset  $\theta_{\text{off}} \approx \pm 4^\circ$  to provide the required distance between the concentrated radiant beam and the dish's center axis  $R_f = 200$  mm. For design C, the dish's optical axis and center axis (see definition in Fig. 1) are parallel but radially displaced by  $R_f$ , similar to the design presented by Schmitz et al. (2017b), in such a way that the focal point moves on a circle of radius  $R_f$  as the primary dish rotates around the center axis. Design D uses the same primary parabolic dish as A and B but incorporates a tilted flat secondary reflector to fold the primary's focal point down and off-axis. Analogous to design C, the focal point moves along a circle of radius  $R_f$  as the secondary reflector rotates around the optical axis. Note that the outline of the secondary reflector is elliptic, corresponding to the intersection of a tilted plane with a cone with the primary's rim as base and the apex slightly above the primary's focal point. To ensure full collection by the secondary, the position of the apex is determined by the edge rays assuming geometrical inaccuracies of the parabolic dish. Designs E and F are based on the same optical principle as D, however the secondary reflector is a hyperboloid according to the Cassegrain design (Mauk et al., 1979), with one of its focal points coincident with the primary's focal point and the second one located on the solar reactor's aperture. The hyperbolic shape allows to move the focal point closer towards the primary without increasing the secondary's size, potentially even behind the primary reflector for easier accessibility of the solar reactors. In the example considered here, the secondary focus is placed at the vertex of the parabola which however reduces the final beam angle of the

radiation to  $\phi_2 = 30^\circ$  after the reflection at the secondary. This inherently leads to lower concentrations because of conservation of étendue. The difference between designs E and F results from the primary parabolic dish rim angle with  $\phi_1 = 45^\circ$  and  $\phi_1 = 90^\circ$  respectively. Thanks to the large rim-angle of the parabolic primary  $\phi_1 = 90^\circ$ , design F represents by far the most compact design. Just as B, design G uses a tracking offset  $\theta_{\text{off}} = \pm 4^\circ$  to shift the focus. To eliminate coma, its shape is derived using the 2D simultaneous multiple surface (SMS) method (Chaves, 2008; Miñano and González, 1992) which guarantees that off-axis radiation incoming at  $\theta_{\text{off}} = \pm 4^\circ$  is focused on the reactor apertures at  $R_f = \pm 200$  mm. Both primary and secondary reflectors are revolved freeform curves and interdependent, meaning that the primary alone does not form a focal spot. Not considered here is the 3D SMS design (Benitez et al., 1999).

Optical performance was evaluated by Monte Carlo ray-tracing  $10^7$  rays using LightTools (Synopsys Inc, 2015). Fig. 2 shows the mean solar concentration ratio and incident solar radiative power versus the solar reactor's aperture radius. A direct normal irradiance of  $E_{\text{bn}} = 1000 \text{ W m}^{-2}$  with spatially uniform distribution over the dish inlet aperture and  $\theta_{\text{sun}} = 4.65$  mrad was assumed. A reflectance of  $\rho = 90\%$  and Gaussian surface normal error distribution with a standard deviation of  $\sigma = 3.5$  mrad ( $\sim 0.2^\circ$ ) were selected (Shuai et al., 2008; Ulmer et al., 2009). For all designs, an inner circle of radius  $R_i = 400$  mm was assumed to be shaded by the solar reactors and, for designs D-G, additionally shading by the secondary reflector is included. Table 1 lists the peak solar concentration ratio  $C_{\text{peak}}$  and the mean solar concentration ratio  $C_{\text{mean}} = \dot{Q}_{\text{reactor}} / (A_{\text{reactor}} E_{\text{bn}})$ , where  $A_{\text{reactor}}$  is the area of a 30 mm-radius aperture.

Designs A and C achieve the best performance:  $C_{\text{mean}} = 4200$  suns and  $\dot{Q}_{\text{reactor}} = 11.8 \text{ kW}$  are achieved over a 30 mm-radius aperture with both designs. The introduction of a tracking offset as proposed in design B results in significantly lower  $C_{\text{mean}}$  and  $\dot{Q}_{\text{reactor}}$  due to comatic aberration inherent of parabolic concentrators as compared to A and C, especially for small aperture radii. For example, for a reactor's aperture

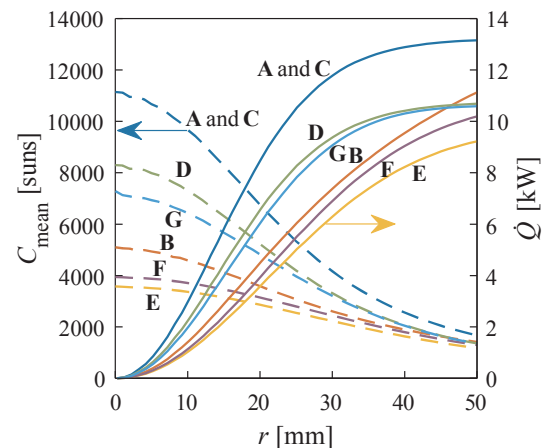


**Fig. 2.** Mean solar concentration ratio (dashed lines) and incident solar radiative power (solid lines) as a function of the solar reactor's aperture radius.





53.9°, and projected total and illuminated area of 15.3 m<sup>2</sup> and 12.9 m<sup>2</sup>, respectively. For the 30 mm aperture of the solar reactors, the full system achieves a geometric concentration ratio of  $C_{\text{geo}} = A_{\text{dish}}/A_{\text{reactor}} = 4560$ . The relatively shorter focal length compared to design D in the previous chapter ( $f = 2.2$  m instead of  $f = 2.65$  m) provides compactness. For both primary and secondary reflectors, 160 × 160 × 1 mm highly reflective back-silvered float-glass reflectors (Fast Glass, 2017) were glued onto the support structure.

The secondary planar reflector has an area  $A_2 = 1.71$  m<sup>2</sup> and tilt angle  $\beta/2 = 12^\circ$ . It was designed and positioned such that all rays coming from the primary reflector are intercepted and directed to the focal point which is displaced by  $R_f = 0.2$  m from the primary optical axis. The outline of the planar secondary is given by the intersection of a tilted flat plane and a cone with the dish's rim as the base and the apex slightly above the primary focal point. The apex is positioned such that radiation deviating up to 0.5° (8.73 mrad) away from the focal point is still intercepted, accounting for the solar angular subtense of 4.65 mrad as well as for tracking errors and primary shape inaccuracies. The tilt of the secondary reflector  $\beta/2$ , where  $\beta$  is the angle between the primary and secondary optical axes, is determined by the distance  $R_f$  by which the focus needs to be displaced and its distance to the focal point. A larger tilt places the secondary closer to the focal point, while a lower tilt moves it further away.  $\beta$  was chosen to minimize losses caused by shading and blocking in the system. The yellow dotted lines in Fig. 4 indicate the three regions prone to shading and blocking: (1) shading of the primary reflector by the secondary reflector, (2) blocking between primary and secondary reflectors by instruments, and (3) blocking between secondary reflector and focus by instruments. For configurations with no collisions between secondary reflector and instruments, the size of the secondary reflector decreases with increasing tilt angle, therefore leading to lower losses by shading but at the expense of higher losses by blocking. The optimum was found for  $\beta = 24^\circ$ , which results in a relatively large secondary reflector with 11.1% shading losses and 1.7% blocking losses.

While the primary reflector is exposed to DNI only, the secondary reflector needs to withstand concentrated irradiance. Fig. 5 shows the spatial distribution of the solar concentration ratio incident on the secondary reflector obtained by ray-tracing simulation, assuming  $\rho_1 = 90.0\%$  and a primary reflector slope error of 3.5 mrad. The solar concentration peaks at 20.0 suns and drops to zero towards the rim. It also drops to zero towards the central area because of shading and blocking by the secondary itself as well as by the solar reactors. Further noticeable are the shades of the 8 rods of the mounting structure of the secondary reflector and very faintly the gaps between the 12 individual panels of the primary reflector. For  $E_{\text{bn}} = 1 \text{ kW m}^{-2}$ , the total radiative power absorbed by the secondary reflector is estimated to be 1.13 kW for an absorptance of  $\alpha_2 = 10\%$ .

All instruments are mounted on a common instrument holder fixed axially at the center of the primary parabolic dish concentrator. The

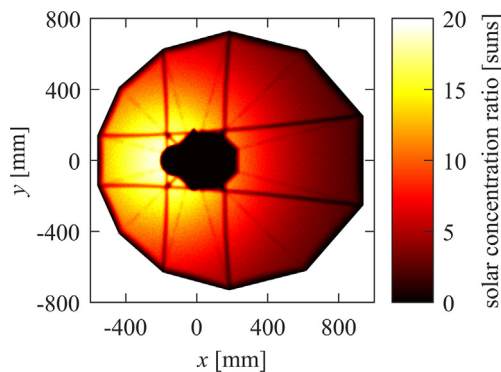


Fig. 5. Spatial distribution of the solar concentration ratio incident on the secondary reflector.

solar reactors, the water calorimeter, and the Lambertian target are tilted by  $\beta = 24^\circ$  and with their aperture's centers positioned along the circular focal point trajectory as the secondary rotates (see red dashed circle in Fig. 3b). An accurate focal position is guaranteed by two-axis tracking (azimuth/altitude) using two three phase AC motors (Lenze IE1 MD071) which follows a pre-calculated path (Reda and Andreas, 2004). The dish's orientation is then fine-tuned using a solar sensor (Solar MEMS ISS-D5, precision = 0.005°). The secondary reflector is rotated using a slotless, brushless rotary motor (Aerotech BMS60).

#### 4. Characterization methodology

The most important quantity to be determined is the solar radiative power incident at the solar reactor's aperture  $\dot{Q}_{\text{reactor}}$ . Here we apply two independent methods to measure  $\dot{Q}_{\text{reactor}}$ , namely: an optical method based on a calibrated CCD camera recording the image on a Lambertian target, and a water-cooled calorimeter. The optical efficiency  $\eta_{\text{opt}}$  is defined as

$$\eta_{\text{opt}} = \frac{\dot{Q}_{\text{reactor}}}{\dot{Q}_{\text{dish}}} = \frac{\dot{Q}_{\text{reactor}}}{A_{\text{dish}} E_{\text{bn}}} = \rho_1 \zeta_1 \rho_2 \zeta_2 \gamma \quad (1)$$

where  $\dot{Q}_{\text{dish}}$  is the incident radiant power on the dish aperture,  $A_{\text{dish}}$  is the dish aperture area,  $E_{\text{bn}}$  the DNI,  $\rho_1$  and  $\rho_2$  are the reflectance of primary and secondary reflectors,  $\zeta_1$  and  $\zeta_2$  are the active area fractions of primary and secondary reflectors, and  $\gamma$  is the intercept factor of a given area on the focal plane (Rabl, 1985). For our system,  $A_{\text{dish}} = 12.9 \text{ m}^2$  is the illuminated area of the primary dish, excluding  $A_{\text{shaded}} = 2.4 \text{ m}^2$  that is shaded by the secondary reflector and its support structure.  $E_{\text{bn}}$  is measured using a pyrheliometer (EKO Instruments MS-56). The measured averaged spectral hemispherical reflectance for primary and secondary reflectors are  $\rho_1 = 94.0\%$  and  $\rho_2 = 94.3\%$  (see Appendix A). The active area fraction of the primary reflector  $\zeta_1 = 96.2\%$  accounts for the gaps between the individual panels (0.8% loss) and the 2.5 mm spacing between the 160 mm × 160 mm reflector segments (3.1% loss). For the secondary reflector, a smaller 0.3 mm spacing was chosen (0.5% loss) to diminish absorption and limit heating, as only free convection is used for cooling. Between the primary reflector and the secondary reflector, blocking losses due to the instruments depend on the position of the secondary. Thus, the total active area fraction of the secondary reflector  $\zeta_2 = 97.8, 97.4$ , and  $97.5\%$  for the case the focus is on the solar reactors, Lambertian target, or water calorimeter, respectively.

The optical methodology developed by Schubnell et al. (1991) is applied to determine the spatial distribution of the incident solar radiative flux. An Al<sub>2</sub>O<sub>3</sub> plasma-coated Lambertian (diffusely-reflective) and water-cooled 200 mm × 200 mm target is mounted at the focal plane and the image is recorded by a calibrated CCD camera (Basler scA1400-17gm) with a manual zoom lens (RICOH FL-CC6Z1218-VG) protected by neutral density filters (ND 4.8). The solar radiative power is then obtained by numerical integration of the solar power flux over a given area. This value is equivalent to:

$$\dot{Q} = \rho_1 \rho_2 \zeta_1 \zeta_2 \gamma A_{\text{dish}} E_{\text{bn}} \quad (2)$$

where  $\gamma$  is the corresponding intercept factor. For the calibration of the camera (Ulmer et al., 2002), we use the total radiative power incident on the target, assuming no spillage (intercept factor  $\gamma = 1$ ). For the solar power input to the solar reactor, we integrate the flux over a 30 mm-radius circular area, corresponding to the solar reactor's aperture.

We can also use the flux distribution on the target to assess the reflector slope error. For this we perform ray-tracing and apply Gaussian scattering on the reflectors. The corresponding standard deviation of the Gaussian distribution  $\sigma$  in the ray tracing can be found with a parameter sweep in which the intercept factor for the 30 mm-radius aperture is matched to experimental data.

To verify the optical measurements, we use a water-cooled

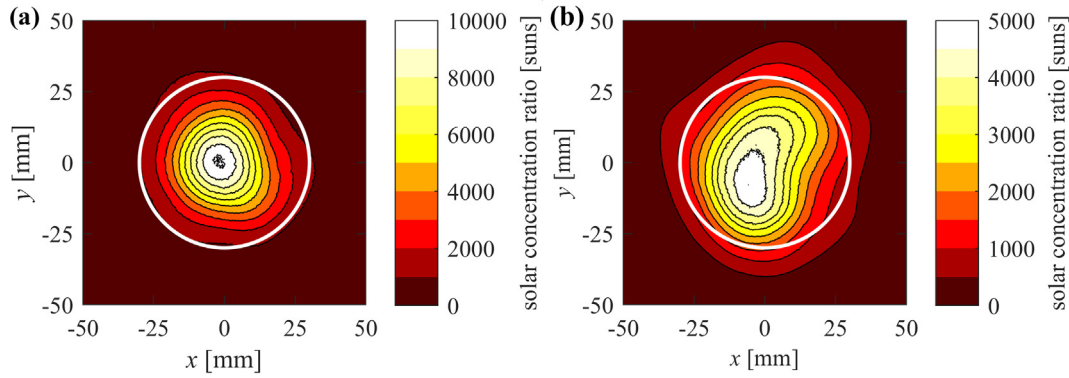


**Fig. 6.** Solar concentration ratio distribution measured for: (a) the stand-alone primary dish concentrator; and (b) the complete system including secondary reflector. The white circle indicates the 30-mm-radius circular area, which corresponds to the size of the solar reactor's aperture.

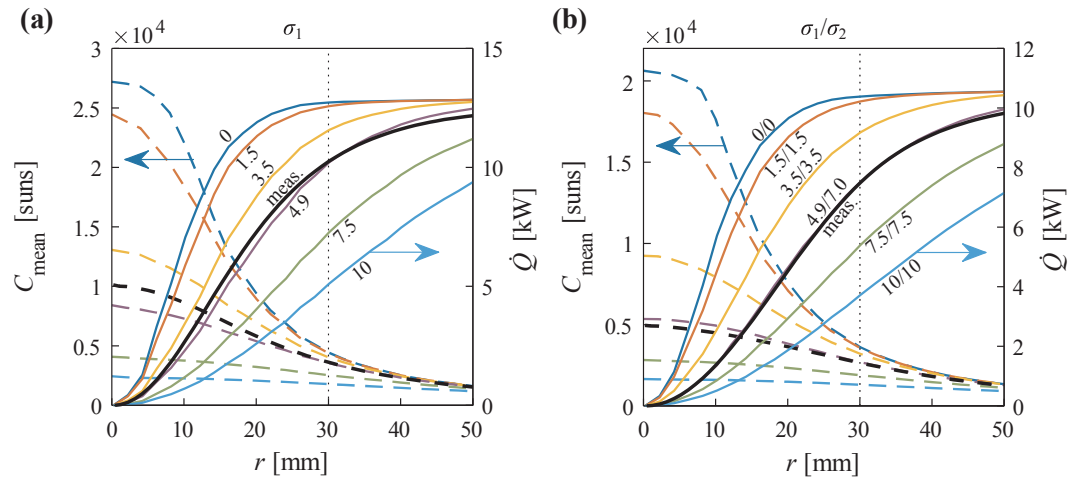


**Fig. 7.** Mean solar concentration ratio and solar radiative power ( $E_{bn} = 1 \text{ kW/m}^2$ ) versus the aperture radius for: (a) the stand-alone primary dish concentrator; and (b) the complete system including secondary reflector. Results are plotted for measured data (bold black line) and ray-tracing simulated data (thinner colored lines) using standard deviations of the slopes  $\sigma_1 = 0, 1.5, 3.5, 4.9$  (matched to measured curve) 7.5 and 10 mrad for case (a), and with  $\sigma_1/\sigma_2 = 0/0, 1.5/1.5, 3.5/3.5, 4.9/7.0$  (matched to measured curve), 7.5/7.5, 10/10 mrad for case (b).

calorimeter. It consists of a well-insulated cavity with an aperture of 30 mm-radius, equal to the solar reactor's aperture. Its inner surfaces are lined with a coiled copper tube for the water flow. The tube surface is coated with  $\text{Al}_2\text{O}_3$ -40%  $\text{TiO}_2$  with measured solar-averaged hemispherical reflectance  $\rho_{\text{coating}} = 8.0\%$  (Appendix A). Ray-tracing simulations with an in-house software code (Petrusch, 2010) indicate an apparent absorptance  $\alpha_{\text{cal}} = 99.5\%$ . The calorimeter determines the radiant power through its aperture by measuring the inlet temperature  $T_{\text{in}}$  and outlet temperature  $T_{\text{out}}$  as well as the mass flow rate  $\dot{m}$  of the cooling water. The power absorbed by the cooling water is given by  $\dot{Q}_{\text{water}} = \dot{m}c_p(T_{\text{out}} - T_{\text{in}})$ , where  $c_p$  is the specific heat of water. Other heat sinks and sources were considered (Groer and Neumann, 1999), e.g. reflection/emission through the aperture, conduction through the insulation, convection through aperture, and heat gains through friction of the cooling water, but these were found to be negligible. Thus, the solar radiative power intercepted by the calorimeter  $\dot{Q}_{\text{cal}} = \dot{Q}_{\text{water}}/\alpha_{\text{cal}}$ .

## 5. Results and discussion

Measurements were performed for two cases: (a) the stand-alone primary dish concentrator; and (b) the complete system including secondary reflector. Fig. 6 shows the measured solar concentration ratio distribution on the Lambertian target for both cases. For case (a),  $C_{\text{peak}} = 10,160$  suns peak and  $C_{\text{mean}} = 3630$  suns over a 30 mm-radius

**Table 2**

Breakdown of optical efficiency into the contributions by reflectance, active area fraction, and intercept factors of primary and secondary reflectors.

Quantity	Current system	Improved system
Primary reflector		
Active area fraction $\zeta_1$	96.2%	99.5%
Reflectance $\rho_1$	94.0%	94.0%
Secondary reflector		
Active area fraction $\zeta_2$	97.8%	97.8%
Reflectance $\rho_2$	94.3%	94.3%
Focal plane		
Intercept factor $\gamma$	71.4%	95.7%
Optical efficiency $\eta_{\text{opt}}$	59.6%	82.3%

circular area. For case (b):  $C_{\text{peak}} = 5010$  suns peak and  $C_{\text{mean}} = 2660$  suns over a 30 mm-radius circular area. Integration of  $C$  over that area and normalized to  $E_{bn} = 1 \text{ kW m}^{-2}$  yields  $\dot{Q} = 10,260 \text{ W}$  and  $7520 \text{ W}$  for the cases (a) and (b), respectively. The corresponding intercept factor is  $\gamma = 78.8$  and  $70.3\%$ , respectively. The main reasons for the decrease in performance for case (b) are: (1) the introduction of the additional reflection ( $\rho_2 = 94.3\%$ ) as well as angular scattering due to reflector slope errors resulting in a lower intercept factor; and (2) the inlet aperture of the primary reflector is reduced from  $15.0 \text{ m}^2$  to

$12.9 \text{ m}^2$  due to shading by the secondary reflector and its support structure. Since the shading occurs in the center of the parabolic dish, which is most tolerant to slope errors, it also negatively affects the intercept factor.

To collect a part of the spillage around the 30 mm-radius aperture, a reflective frustum is implemented in front of the focal plane (see Fig. 3b), increasing the intercept factor to  $\gamma = 71.4\%$ . Finally, for the 30 mm-radius aperture,  $\dot{Q}_{\text{reactor}} = 7,680 \text{ W}$  with  $C_{\text{mean}} = 2,710$  suns and  $C_{\text{peak}} = 5,010$  suns. The validity of the optical measurements is confirmed by comparison with the water calorimeter measurements. The relative difference between the two independent methods is 0.7%.

Fig. 7 shows  $C_{\text{mean}}$  and  $\dot{Q}$  versus the aperture radius for both cases. The bold black lines indicate the measured data. The thinner colored lines represent the ray-tracing simulation results using standard deviations of the slopes  $\sigma_1 = 0, 1.5, 3.5, 4.9$  (matched to measured curves) 7.5 and 10 mrad for case (a), and with  $\sigma_1/\sigma_2 = 0/0, 1.5/1.5, 3.5/3.5, 4.9/7.0$  (matched to measured curve), 7.5/7.5, 10/10 mrad for case (b). Evidently,  $C_{\text{mean}}$  and  $\dot{Q}$  drop with increasing  $\sigma$ . Although the actual error is not perfectly Gaussian, the ray-tracing simulations provide a good indicator for the reflector quality. We attribute an error  $\sigma_1 = 4.9$  mrad to the primary dish concentrator by matching the measured and simulated 30-mm-radius intercept factor for case (a). Discrepancies are mainly due to imperfect alignment of the 12 panels, which was not simulated. Having fixed a value for  $\sigma_1$ , we attribute  $\sigma_2 = 7$  mrad by matching measured and simulated data for case (b). The source of this error is mainly attributed to imperfect planarity and alignment of the secondary reflector. Table 2 lists the breakdown of optical efficiency into the contributions by reflectance, active area fraction, and intercept factors of primary and secondary reflectors for the measured values. The main source of losses occurs at the interception of the rays due to the slope error of the reflectors ( $\sigma_1 = 4.9$  mrad,  $\sigma_2 = 7.0$  mrad) and the larger rim angle chosen to increase compactness. Ray-tracing

simulations with an improved setup where these imperfections could be reduced, assuming  $\sigma_1 = \sigma_2 = 1.5$  mrad to account for surface (Stalcup et al., 2012) and tracking errors, and  $\zeta_1 = 99.5\%$  to account for smaller gaps in-between the mirror segments, yield  $\eta_{\text{opt}} = 82.3\%$ .

## 6. Conclusion

Various optical configurations were analyzed for the design of a high-flux solar dish system that alternates the focus of concentrated solar radiation between two solar redox reactors. The design comprising a two-axis tracking primary parabolic dish coupled to a secondary rotating planar reflector was selected for further analysis and subsequently for construction because of its good combination of optical performance, simplicity, robustness, and manufacturability. The fabricated system was optically characterized by optical measurements and verified with a water-cooled calorimeter. For a DNI of  $1 \text{ kW m}^{-2}$ , it delivers a solar radiative power of 7680 W to the 30-mm radius aperture of the solar reactor with a mean and peak solar concentration ratio of 2710 suns and 5010 suns, respectively, yielding an overall optical efficiency of 59.6%. Detailed optical analyses based on experimentally measured and numerically simulated data identify measures to increase the optical efficiency to 82%.

## Acknowledgements

We gratefully acknowledge the financial support by the Swiss Federal Office of Energy (Grant No. 8100065-01) and the Swiss National Science Foundation (Grant No. 206021\_170735). We thank Andrea Pedretti and Gianluca Ambrosetti from Synhelion SA for their contributions to the optical design and for the delivery of the metallic frame and tracking system of the solar dish.

## Appendix A. . Measurement of spectral hemispherical reflectance

The spectral hemispherical reflectance was measured using the setup described in Coray et al. (2011) with adaptations identical to those made in Schmitz et al. (2017a). An integrating sphere (Labsphere RT-060-SF) was used to perform a relative reflectance measurement with respect to standard reflective samples (Labsphere AS-01161-060 for the reflectors, SphereOptics SG3072 for the coating) according to the comparison method (Jacquez and Kuppenheim, 1955). Radiation was incident on the sample at an angle of  $8^\circ$  distributed within a half angle of 6 mrad. The (diffuse) hemispherical reflectance of several thermal spray coatings for the water calorimeter's cavity was measured:  $\text{Al}_2\text{O}_3$ -40%  $\text{TiO}_2$ ,  $\text{Cr}_2\text{O}_3$ -25%  $\text{TiO}_2$ ,  $\text{TiO}_2$  99% and  $\text{Cr}_2\text{O}_3$  99%. Both primary and secondary reflectors used flat  $160 \times 160 \times 1 \text{ mm}$  back-silvered floated-glass mirrors from Fast Glass Srl (Fast Glass, 2017). Their angular scattering is negligible (Good et al., 2016) and it is therefore sufficient to measure the hemispherical reflectance (Meyen et al., 2013).

Fig. 8 shows the measured spectral hemispherical reflectance for the reflector and the best performing coating  $\text{Al}_2\text{O}_3$ -40%  $\text{TiO}_2$  versus wavelength. The averaged hemispherical reflectance is calculated by the weighted ordinates method, where the spectrum used for the primary reflector is ASTM-G173 direct normal irradiance AM 1.5 (ASTM, 2012). For the reflectance of the secondary reflector and the calorimeter coating, we account for the change in spectrum induced by the reflections at the primary reflector. Table 3 summarizes the values of the spectrally-averaged

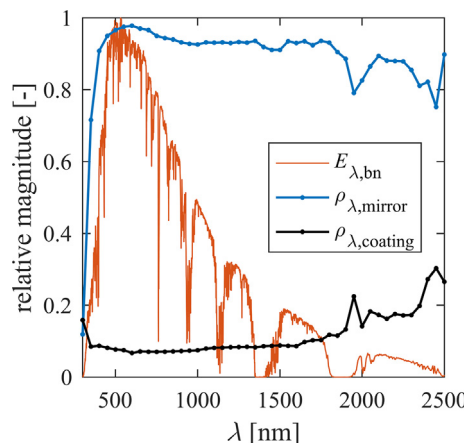


Fig. 8. Normalized solar spectrum and measured spectral hemispherical reflectance versus wavelength.

**Table 3**  
Measured spectrally-averaged hemispherical reflectance of samples.

Spectrum ASTM-G173 AM1.5	Direct	Direct + 1 refl.	Direct + 2 refl.
Reflector	93.98%	94.26%	94.44%
Al <sub>2</sub> O <sub>3</sub> -40% TiO <sub>2</sub>	8.07%	8.01%	7.96%
Cr <sub>2</sub> O <sub>3</sub> -25% TiO <sub>2</sub>	9.46%	9.37%	9.32%
TiO <sub>2</sub> 99%	10.18%	10.09%	10.02%
Cr <sub>2</sub> O <sub>3</sub> 99%	14.77%	14.73%	14.70%

hemispherical reflectance of the samples. The different spectral distributions lead to a slightly increased reflectance of the secondary reflector  $\rho_2 = 94.26\%$  compared to  $\rho_1 = 93.98\%$ , even though the reflectors are identical. For the best performing coating Al<sub>2</sub>O<sub>3</sub>-40% TiO<sub>2</sub> applied to the calorimeter cavity,  $\rho_{\text{coating}} = 7.96\%$  using the spectral distribution after two reflections.

## References

- ASTM, 2012. ASTM E903-12 Standard Test Method for Solar Absorptance, Reflectance, and Transmittance of Materials Using Integrating Spheres. ASTM International, West Conshohocken, PA.
- Benítez, P., Mohedano, R., Minano, J.C., 1999. Design in 3D geometry with the simultaneous multiple surface design method of nonimaging optics. *P Soc. Photo-Opt. Ins.* 3781, 12–21.
- Bliss, R.W., 1957. Notes on performance design of parabolic solar furnaces. *Sol. Energy* 1 (1), 22–29.
- Chaves, J., 2008. Introduction to Nonimaging Optics. CRC Press, Boca Raton.
- Chueh, W.C., Falter, C., Abbott, M., Scipio, D., Furler, P., Haile, S.M., Steinfeld, A., 2010. High-flux solar-driven thermochemical dissociation of CO<sub>2</sub> and H<sub>2</sub>O using non-stoichiometric ceria. *Science* 330 (6012), 1797–1801.
- Coray, P.S., Lipinski, W., Steinfeld, A., 2011. Spectroscopic goniometry system for determining thermal radiative properties of participating media. *Exp. Heat Transfer* 24 (4), 300–312.
- Fast Glass, 2017. Fast Glass Srl. < www.glass.it > (accessed 13 December 2017).
- Good, P., Cooper, T., Querci, M., Wiik, N., Ambrosetti, G., Steinfeld, A., 2016. Spectral reflectance, transmittance, and angular scattering of materials for solar concentrators. *Sol. Energy. Mat. Sol. C* 144, 509–522.
- Groer, U., Neumann, A., 1999. Development and test of a high flux calorimeter at DLR Cologne. *J. Phys. IV* 9 (P3), 643–648.
- Harper, D.A., Hildebrand, R.H., Stiening, R., Winston, R., 1976. Heat trap: an optimized far infrared field optics system. *Appl. Opt.* 15 (1), 53–60.
- Jacquez, J.A., Kuppenheim, H.F., 1955. Theory of the integrating sphere. *J. Opt. Soc. Am.* 45 (6), 460.
- Marxer, D., Furler, P., Scheffe, J., Geerlings, H., Falter, C., Batteiger, V., Sizmann, A., Steinfeld, A., 2015. Demonstration of the entire production chain to renewable kerolene via solar thermochemical splitting of H<sub>2</sub>O and CO<sub>2</sub>. *Energ. Fuel* 29 (5), 3241–3250.
- Mauk, C.E., Prengle, H.W., Sun, E.C.H., 1979. Optical and thermal-analysis of a cassegrainian solar concentrator. *Sol. Energy* 23 (2), 157–167.
- Meyen, S., Montecchi, M., Kennedy, C., Zhu, G., Gray, M., Crawford, J., Hiemer, S., Platzer, W., Heimsath, A., O'Neill, M., Ziegler, S., Brändle, S., Fernandez, A., 2013. Parameters and method to evaluate the solar reflectance properties of reflector materials for concentrating solar power technology – official SolarPACES reflectance guideline version 2.5. SolarPACES.
- Miñano, J.C., González, J.C., 1992. New method of design of nonimaging concentrators. *Appl. Opt.* 31 (16), 3051–3060.
- Panlener, R.J., Blumenthal, R.N., Garnier, J.E., 1975. A thermodynamic study of non-stoichiometric cerium dioxide. *J. Phys. Chem. Solids* 36 (11), 1213–1222.
- Petrash, J., 2010. A free and open source Monte Carlo ray tracing program for concentrating solar energy research. Proceedings of the ASME 4th International Conference on Energy Sustainability, pp. 125–132.
- Rabl, A., 1985. Active Solar Collectors and Their Applications. Oxford University Press, New York.
- Reda, I., Andreas, A., 2004. Solar position algorithm for solar radiation applications. *Sol. Energy* 76 (5), 577–589.
- Romero, M., Steinfeld, A., 2012. Concentrating solar thermal power and thermochemical fuels. *Energ. Environ. Sci.* 5 (11), 9234–9245.
- Scheffe, J.R., Steinfeld, A., 2012. Thermodynamic analysis of cerium-based oxides for solar thermochemical fuel production. *Energ. Fuel* 26 (3), 1928–1936.
- Schmitz, M., Ambrosetti, G., Cooper, T., Steinfeld, A., 2017a. On-sun optical characterization of a solar dish concentrator based on elliptical vacuum membrane facets. *Sol. Energy* 153, 732–743.
- Schmitz, M., Wiik, N., Ambrosetti, G., Pedretti, A., Paredes, S., Ruch, P., Michel, B., Steinfeld, A., 2017b. A 6-focus high-concentration photovoltaic-thermal dish system. *Sol. Energy* 155, 445–463.
- Schubnell, M., Keller, J., Imhof, A., 1991. Flux density distribution in the focal region of a solar concentrator system. *J. Sol. Energy Eng.* 113 (2), 112.
- Shuai, Y., Xia, X.L., Tan, H.P., 2008. Radiation performance of dish solar concentrator/cavity receiver systems. *Sol. Energy* 82 (1), 13–21.
- Stalcup, T., Angel, J.R.P., Coughenour, B., Wheelwright, B., Connors, T., Davison, W., Lesser, D., Elliott, J., Schaefer, J., 2012. On-sun performance of an improved dish-based HCPV system. *Proc. SPIE* 8468.
- Synopsys Inc, 2015. LightTools 8.3.2.
- Ulmer, S., Heinz, B., Pottler, K., Lupfert, E., 2009. Slope error measurements of parabolic troughs using the reflected image of the absorber tube. *J. Sol. Energy. – T ASME* 131 (1).
- Ulmer, S., Reinalter, W., Heller, P., Lupfert, E., Martinez, D., 2002. Beam characterization and improvement with a flux mapping system for dish concentrators. *J. Sol. Energy. – T ASME* 124 (2), 182–188.
- Winston, R., 1970. Light collection within the framework of geometrical optics\*. *J. Opt. Soc. Am.* 60 (2), 245.